ELSEVIER

International Journal of Heat and Fluid Flow 19 (1998) 418–430

International Journal of
HEAT AND
FLUID FLOW

Computation of film cooling of a flat plate by lateral injection from a row of holes

D. Lakehal [1], G.S. Theodoridis [2], W. Rodi *

Institute for Hydromechanics, University of Karlsruhe, Kaiserstrasse 12, D-76128 Karlsruhe, Germany

Abstract

Film cooling effectiveness of a flat plate by a row of laterally injected jets is investigated using a Navier–Stokes equation solver which employs a finite-volume method with a multi-block technique. The paper compares measured and calculated temperature and velocity fields obtained with the standard k–ε and the k–ε based two-layer turbulence model for various blowing rates. The resolution of the viscosity-affected near-wall region with a one-equation turbulence model yielded a noticeable improvement in the prediction of film-cooling effectiveness compared to results obtained with wall functions. Furthermore, results of additional calculations using the ad hoc correction proposed by Bergeles et al. (1978), which attempts to promote the lateral diffusivity, combined with the two-layer model indicate that this anisotropy correction enhances indeed the spanwise spreading, but its application very close to the wall needs additional calibration.

Keywords: Film cooling; Two-layer model; Lateral injection

1. Introduction

The thermal performance of modern gas turbines, used either in aircraft engines or power-production systems, depends primarily on the level of temperature at the inlet to the turbine section. Despite the noticeable progress in blade-metallurgy, a reasonable lifetime of turbine blades can be ensured only by an efficient surface-cooling mechanism. Film cooling is one of the most efficient cooling methods; it is generally more efficient than internal convection cooling because of the relatively poor heat-transfer characteristics of air. In film cooling, cool air is discharged from rows of holes to form a thin film on the surface acting as a buffer between the hot gas and the blade. The efficiency of such a technique can be influenced by several parameters, among them the discharge geometry, ejection angle, blowing rate, blade geometry, density and temperature ratio, and reliable prediction methods are needed to optimize the design. In practice often lateral injection is used since with this the cooling film covers better the area to be cooled. The present paper aims to contribute to the development of a prediction method for this situation and to the understanding of the cooling behaviour.

The test case studied here represents film cooling of a flat plate by a row of laterally injected jets. The on-coming flow is that of a fully turbulent boundary layer, and the flow configuration is displayed in Fig. 1. The test case was studied experimentally in detail by Honami et al. (1992). In their experimental investigation, the authors have measured simultaneously velocity and temperature fields using a double-wire probe. The tests were conducted at three mass flux ratios $M = \rho_j U_j / \rho_s U_s = 0.5$, 0.85 and 1.2, ($U_j$ and ρ_j are respectively the injected-jet velocity and density and U_s and ρ_s the primary-stream velocity and density). Although this configuration has a simple geometry, it offers most of the complex features observed in turbo-machinery flows, such as the strongly three-dimensional nature of the flow and temperature field, caused by the interaction between the primary and coolant streams. Also, the lateral injection causes an asymmetric behaviour of the flow. In all cases, the temperature difference between primary stream and coolant was 55°.

Two-equation turbulence models employing wall-functions as near-wall treatment bridging the viscous sublayer are known to be inaccurate in predicting certain flows, in particular when heat transfer is involved. The assumptions on which such near-wall treatment is based are not generally valid; an example is the case in which secondary flows extend into the sublayer (Rodi, 1991). Resolving the viscous sublayer by Low Reynolds number k–ε models was found to require very high numerical resolution near the walls, in order to deal with the steep gradients of the dissipation rate ε. As an alternative, the two-layer approach has recently become popular, in which only the core flow outside the viscosity-affected near-wall region is simulated by the k–ε model. The viscous sublayer is resolved by a simpler model, notably a one-equation model in which the length-scale distribution is prescribed and an ε-equation is not solved. Such models therefore require considerably fewer grid points in the viscous sublayer and are hence more suitable for complex situations involving more

* Corresponding author. E-mail: rodi@ifh.bau-verm.uni-karlsruhe.de.

[1] Present address: HFI, Technical University of Berlin, Germany.

[2] Present address: University of Thessaloniki, Greece.

0142-727X/98/$ – see front matter
PII: S0142-727X(98)10022-X

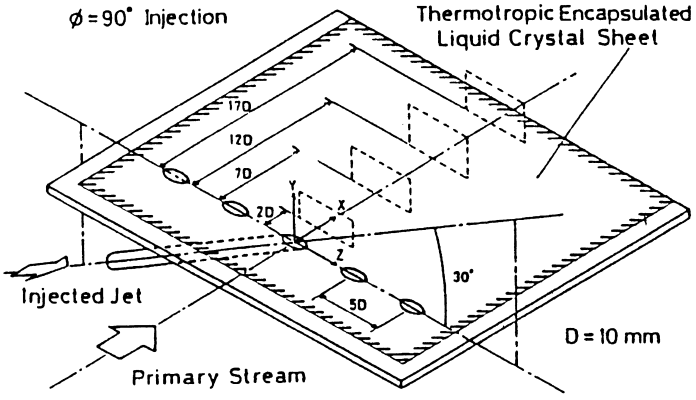

Fig. 1. Experimental apparatus from Honami et al. (1992).

than one wall for which the near-wall regions have to be resolved. Also, because of the fixed length-scale distribution near the wall, these models have been found to give better predictions for adverse pressure gradient boundary layers than pure k–ε models. In jet-in-a-cross-flow situations, isotropic eddy viscosity/diffusivity models are known to underpredict the lateral spreading of the jet and of passive scalars. Hence, the ad hoc measure proposed by Bergeles et al. (1978), which attempts to increase the lateral eddy viscosity and diffusivity, combined here with the two-layer model, is tested in further calculations.

2. Mean-flow and turbulence-model equations

In three-dimensional, steady, incompressible turbulent flow the mean-flow and temperature field is governed by the following equations written in Cartesian coordinates and conservative form:

$$\frac{\partial}{\partial x_j}\left(\rho u_j \phi + D_j^{\phi}\right) = S_{\phi}, \tag{1}$$

where ϕ is the time-averaged variable considered (equal to 1 for continuity equation, equal to velocity components u_i for momentum equations, and equal to enthalpy $h = CpT$ for the temperature determining equation). p is the pressure and ρ the fluid density. D_j^{ϕ} and S_{ϕ} denote the diffusion and source terms, respectively, which are given for each variable considered in Table 1. In the momentum and enthalpy equations expressed by Eq. (1), the originally appearing turbulent stresses $\overline{u_i' u_j'}$ and heat fluxes $\overline{u_i' h'}$ are related, respectively, to the mean-velocity and temperature gradients through the eddy-viscosity/diffusivity concept. The distribution of the eddy viscosity μ_t appearing in the equations is calculated with either the standard k–ε model of Launder and Spalding (1974) or the two-layer model described in Rodi (1991). The k–ε model characterises the local state of turbulence through the turbulent kinetic energy ($k = 1/2\,\overline{u_i' u_i'}$) and its rate of dissipation (ε). The standard model applicable to high Reynolds number situations employs the following relation for determining the isotropic eddy viscosity μ_t:

$$\mu_t = C_{\mu}\rho k^2/\varepsilon. \tag{2}$$

The distributions of k and ε are determined from model transport equations which can also be expressed in the form of Eq. (1), with the terms given in Table 1. P_k represents the rate of production of turbulent kinetic energy resulting from the interaction of the turbulent stresses and the mean velocity gradients:

$$P_k = \mu_t\left(\frac{\partial u_i}{\partial x_j} + \frac{\partial u_j}{\partial x_i}\right)\left(\frac{\partial u_i}{\partial x_j}\right). \tag{3}$$

Standard values are assigned to the constants appearing in the turbulence model, namely $C_{\mu} = 0.09$; $C_{\varepsilon 1} = 1.44$; $C_{\varepsilon 2} = 1.92$; $\sigma_k = 1$, and $\sigma_{\varepsilon} = 1.3$. The laminar and turbulent Prandtl numbers Pr and σ_h appearing in the enthalpy equation are set to the values 0.7 and 0.9, respectively.

The two-layer approach adopted here consists of resolving the viscosity-affected regions close to walls with a one-equation model, while the outer core flow is resolved with the standard k–ε model described above. In the one-equation model, the eddy viscosity is made proportional to a velocity scale and a length scale l_{μ}. The distribution of l_{μ} is prescribed algebraically while the velocity scale is determined by solving the k-equation (Eq. (1)). The dissipation rate ε appearing as sink term in the k-equation is related to k and a dissipation length scale l_{ε} which is also prescribed algebraically. The different two-layer versions available in the literature differ in the use of the velocity scale and the way l_{μ} and l_{ε} are prescribed. It should be mentioned that in the fully turbulent region the length scales l_{μ} and l_{ε} vary linearly with distance from the wall. However, in the viscous sublayer l_{μ} and l_{ε} deviate from the linear distribution in order to account for the damping of the eddy viscosity and the limiting behaviour of ε at the wall. The one-equation model employed is due to Norris and Reynolds (1975) and reads:

Table 1
Terms in the governing equations (1)

ϕ	D_j^{ϕ}	S_{ϕ}
1	0	0
u_i	$-\Gamma_u(\partial u_i/\partial x_j)$	$-\partial p/\partial x_i$
k	$-\Gamma_k(\partial k/\partial x_j)$	$P_k - \rho\varepsilon$
ε	$-\Gamma_{\varepsilon}(\partial \varepsilon/\partial x_j)$	$C_{\varepsilon 1}(\varepsilon/k)P_k - C_{\varepsilon 2}\rho\varepsilon^2/k$
h	$-\Gamma_h(\partial h/\partial x_j)$	0

$\Gamma_u = \mu + \mu_t, \Gamma_k \equiv (\mu + \mu_t/\sigma_k), \Gamma_{\varepsilon} \equiv (\mu + \mu_t/\sigma_{\varepsilon}), \Gamma_h \equiv (\mu/\mathrm{Pr}) + (\mu_t/\sigma_h)$

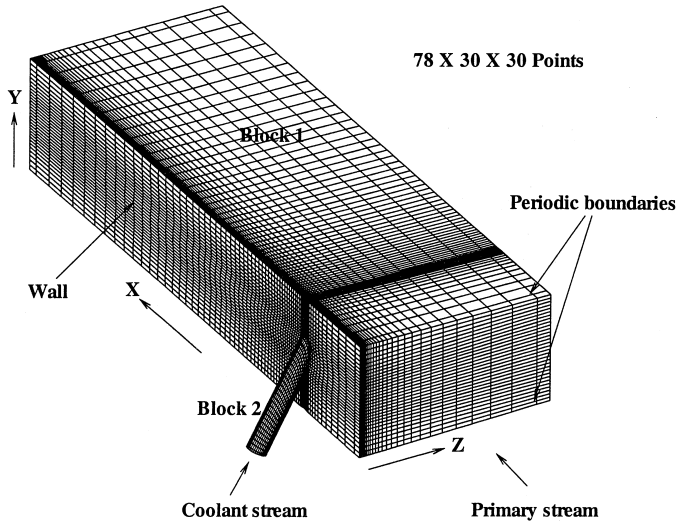

Fig. 2. The computational grid.

$$\mu_t = C_\mu \rho k^{1/2} l_\mu; \quad l_\mu = C_l y_n \underbrace{\left[1 - \exp\left(-\frac{\mathrm{Ry}}{A_\mu}\frac{25}{A^+}\right)\right]}_{f_\mu}, \tag{4}$$

$$\varepsilon = k^{3/2}/l_\varepsilon; \quad l_\varepsilon = \frac{C_l y_n}{1 + 13.2/(\mathrm{Ry} C_l)}. \tag{5}$$

Note that the length scale l_μ is damped in a similar way as the Prandtl mixing length by the Van Driest function, so that it involves an exponential reduction governed by the near-wall Reynolds number $\mathrm{Ry} = \tilde{U} y_n / \nu$. However, in contrast to the original Van Driest function, Ry uses $k^{1/2}$ as a velocity scale $\tilde{U}$ instead of U_τ which can go to zero for separated flows. The constant C_l is set equal to $\kappa C_\mu^{-3/4}$ to conform with the logarithmic law of the wall ($\kappa =$ von Kármán constant). The empirical constants appearing in the damping function are

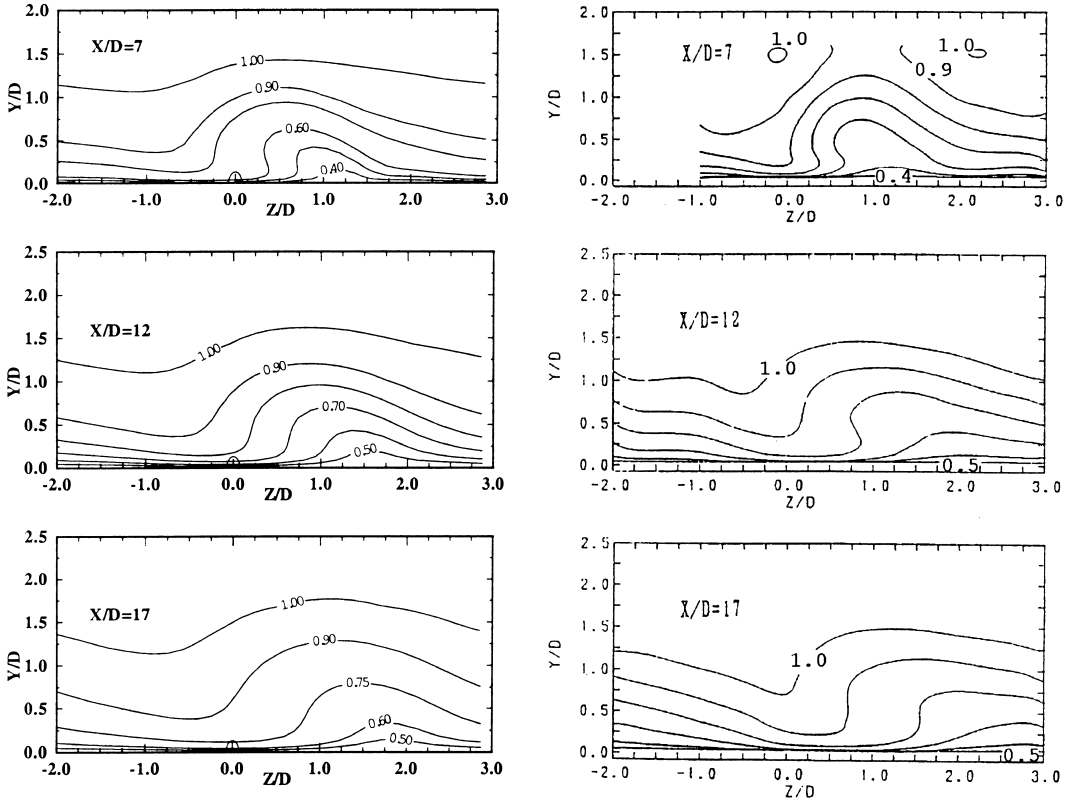

Fig. 3. U-contours; left: calculated; right: experimental $M = 0.50$; k–ε WF.

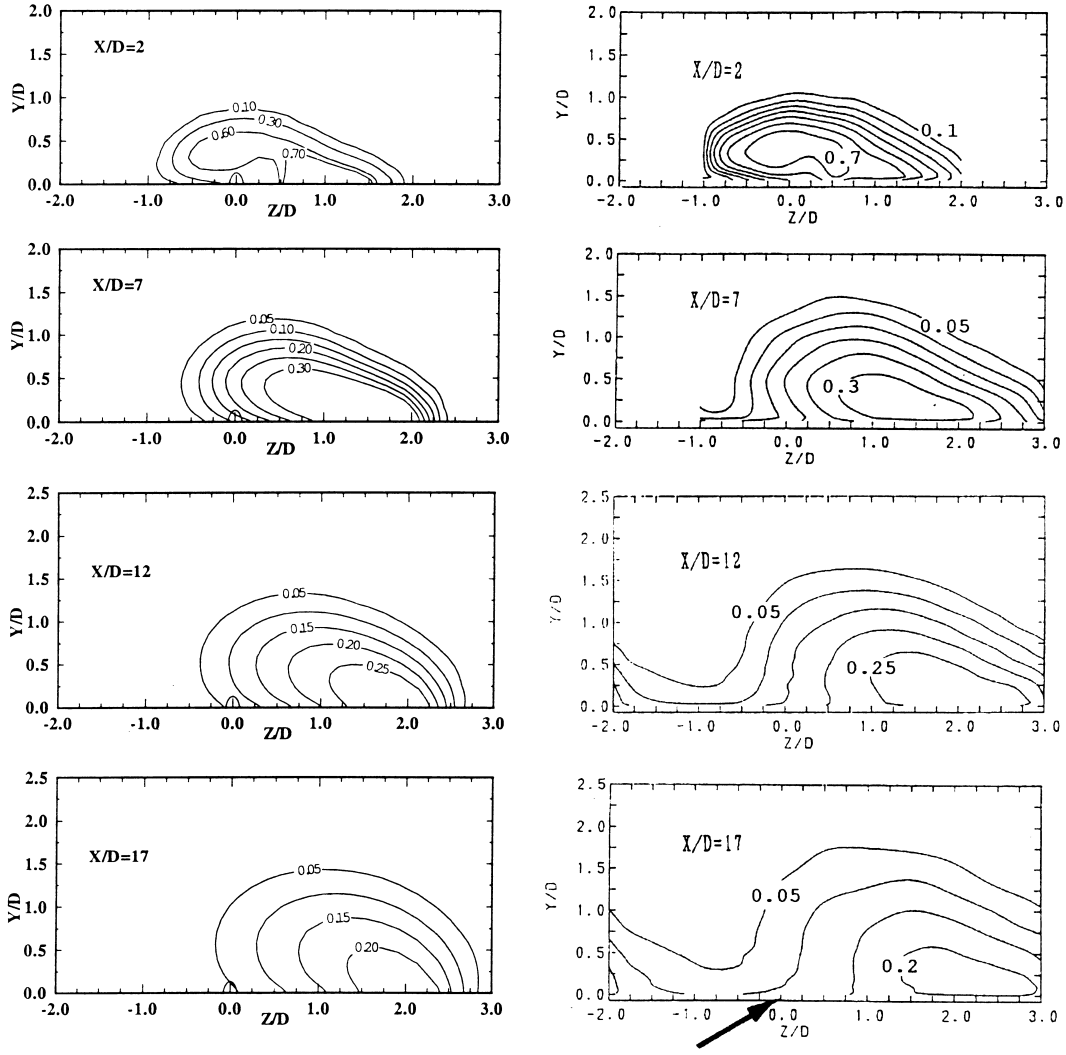

Fig. 4. η-contours; left: calculated; right: experimental $M=0.50$; k–ε WF.

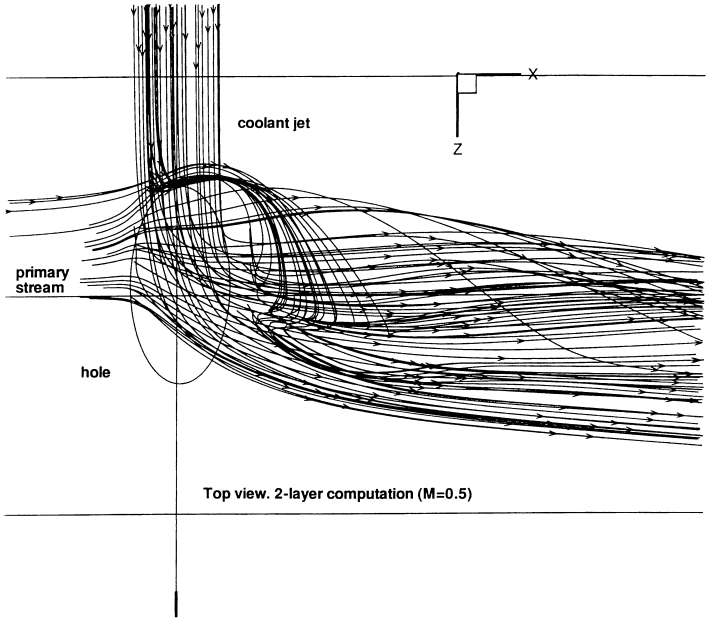

Fig. 5. Streamline patterns near the injection hole; two-layer computations.

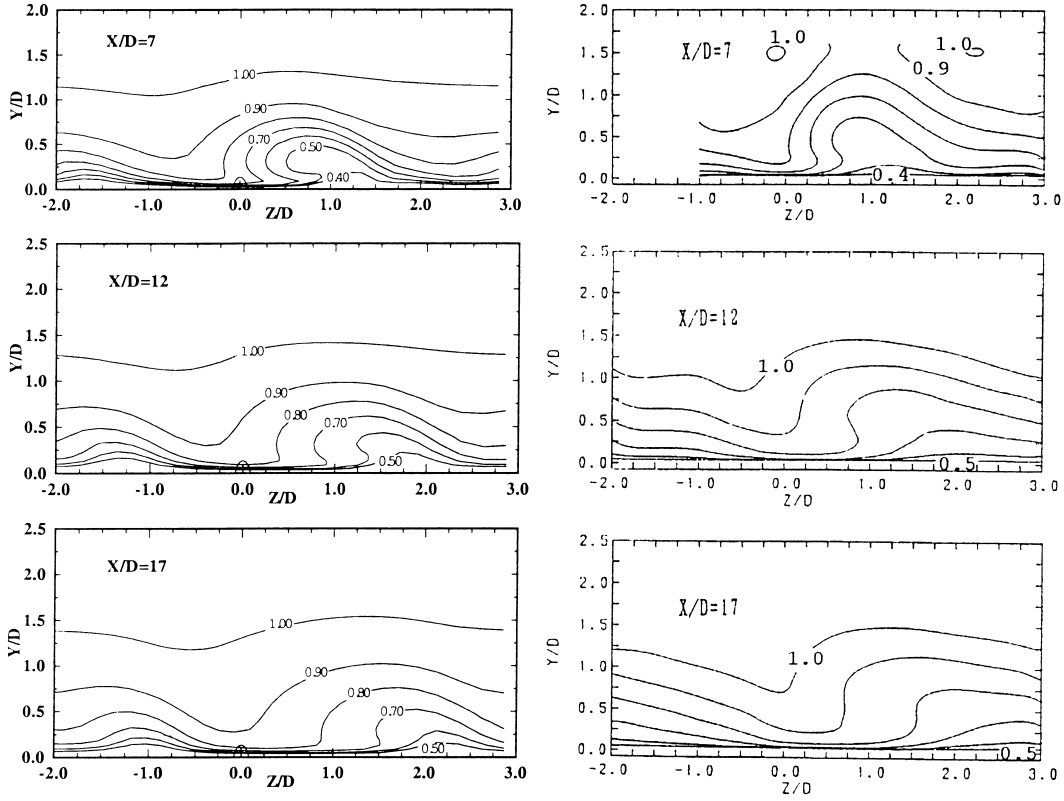

Fig. 6. U-contours; left: calculated; right: experimental $M = 0.50$; k–ε two-layer.

assigned the values $A_\mu = 50.5$ and $A^+ = 25$ (Rodi, 1991). The outer k–ε and the near-wall model are matched dynamically (with no fixed zones) at a location where the damping function (term in brackets) reaches the value 0.95, i.e. where viscous effects become negligible.

Due to the isotropic eddy-viscosity assumption on which two-equation turbulence models are based, computations of jet-in-cross flow, in particular the transport of passive scalars, reveal systematically an under-prediction of the lateral spreading. In order to account for the anisotropy of the turbulent exchange processes in these flows, Bergeles et al. (1978) proposed to substitute the eddy-viscosity μ_t appearing in the lateral components of the Reynolds stresses and scalar fluxes:

$$-\rho\overline{u'w'} = \mu_t \frac{\partial U}{\partial z}; \qquad -\rho\overline{w'\phi'} = \frac{\mu_t}{\sigma_\Phi}\frac{\partial \phi}{\partial z} \tag{6}$$

by an increased value determined by

$$\mu_t^a = \mu_t[1.0 + f(1.0 - y/\delta)], \tag{7}$$

in which μ_t is the eddy viscosity determined by the basic turbulence model. δ denotes the local boundary layer thickness. Relation (7) was derived from model transport equations for the Reynolds stresses by assuming local equilibrium of turbulence and neglecting the stress $\overline{v'w'}$ against $\overline{u'v'}$ and $\overline{u'w'}$. The ratio of eddy viscosities/diffusivities for the stresses and heat fluxes in the lateral and normal direction was found to be equal to the ratio of the fluctuating velocities $\overline{w'^2}/\overline{v'^2}$, which was assumed to vary linearly from a near-wall value f to 1 at the outer edge of the boundary layer. The coefficient f was given the value 3.5 in the original paper. Within the viscous sublayer f may however reach considerably higher values. It should be noted that the above mentioned non-isotropic eddy-viscosity correction was already employed by Demuren et al. (1985) and recently by Zhou et al. (1993) for the prediction of three-dimensional turbulent jets in cross-flow, but limiting its implementation to the lateral components of the Reynolds stresses and heat fluxes in the mean-flow equations. In the present study, the implementation of the correction was extended to all transport equations, and in particular to the diffusion and turbulence production terms appearing in the transport equations for k and ε.

3. The computational method

The numerical procedure applied to calculate the test case is based on a finite-volume approach for solving implicitly the three-dimensional incompressible averaged Navier–Stokes equations on arbitrary non-orthogonal grids, employing a cell-centred grid arrangement. A detailed description of the method is reported in Majumdar et al. (1992). Because of the geometrical complexity of film-cooling problems, a multi-block technique is introduced into this method, which reduces significantly the core memory needed for computation and gives more freedom in generating the grid. This technique allows to generate separately grids for the different parts of the flow domain using a suitable grid generator, namely the region above the blade surface to be cooled, inside the discharge pipe and in the associated plenum if needed. Each block has its

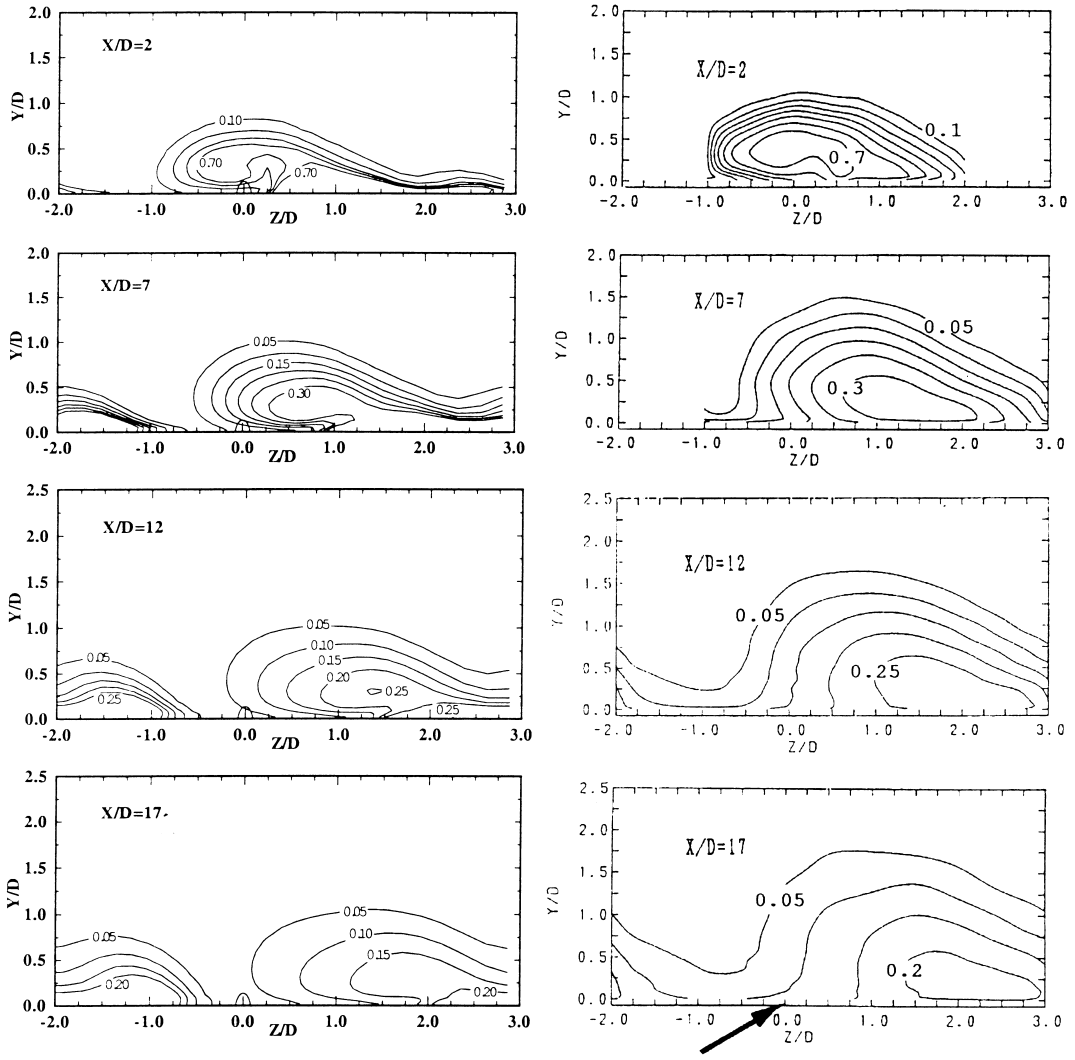

Fig. 7. η-contours; left: calculated; right: experimental $M = 0.50$; k–ε two-layer.

own coordinate system which may not necessarily be of an orientation similar to that of neighbouring blocks. Within a multiblock computational domain, the various blocks are conceptual and the inter-block boundaries have no physical significance. Note that a fundamental requirement of a multiblock method is that the solution of the flow field should be entirely independent of the choice of internal block-boundaries. The individual blocks are connected through the inter-block boundaries, and for each block two additional rows of control volumes are added next to each inter-block boundary. These extended control volumes are placed in such a way that they coincide with the corresponding internal control volumes of the neighbouring block sharing the same inter-block boundary. This overlapping of two rows of control volumes is dictated by the employment of the second order convection schemes. The extended blocks are finally assembled into one array forming the grid for the complete computational domain (see Fig. 2). The computation is performed within each block, with the linkage achieved through special mapping conditions.

The momentum-interpolation technique of Rhie and Chow (1983) is used to prevent pressure-field oscillations which tend to appear in the cell-centred grid arrangement. The pressure–velocity coupling is achieved using the SIMPLEC algorithm of Van Doormal and Raithby (1984), which was found in this case to ensure a better stability than the SIMPLE algorithm. Two different second order schemes were used to approximate the convection fluxes of momentum, heat and k and ε, namely the QUICK scheme of Leonard (1979) and the oscillation-free *Hybrid Linear Parabolic Approximation* scheme (HLPA) developed by Zhu (1991). The achievement of numerical stability when employing the two-layer model has required the application of the HLPA scheme to the k, ε and h-equations, while the momentum equations could be solved with the QUICK scheme. The resulting system of difference equations is solved using the *Strongly Implicit Procedure* (SIP) algorithm of Stone (1968).

The computations performed with the standard k–ε model did not exhibit any convergence difficulties, and the residuals dropped in all cases by five orders for all variables, including k and ε. Convergence was achieved in about 12 min CPU time (around 400 iterations) on the *SNI S*600/20 vector computer. Convergence was not as good for the calculations with the two-layer turbulence model: The computations showed oscillations, in particular in the solution of equations of turbulence qualities for which the residuals remained usually higher

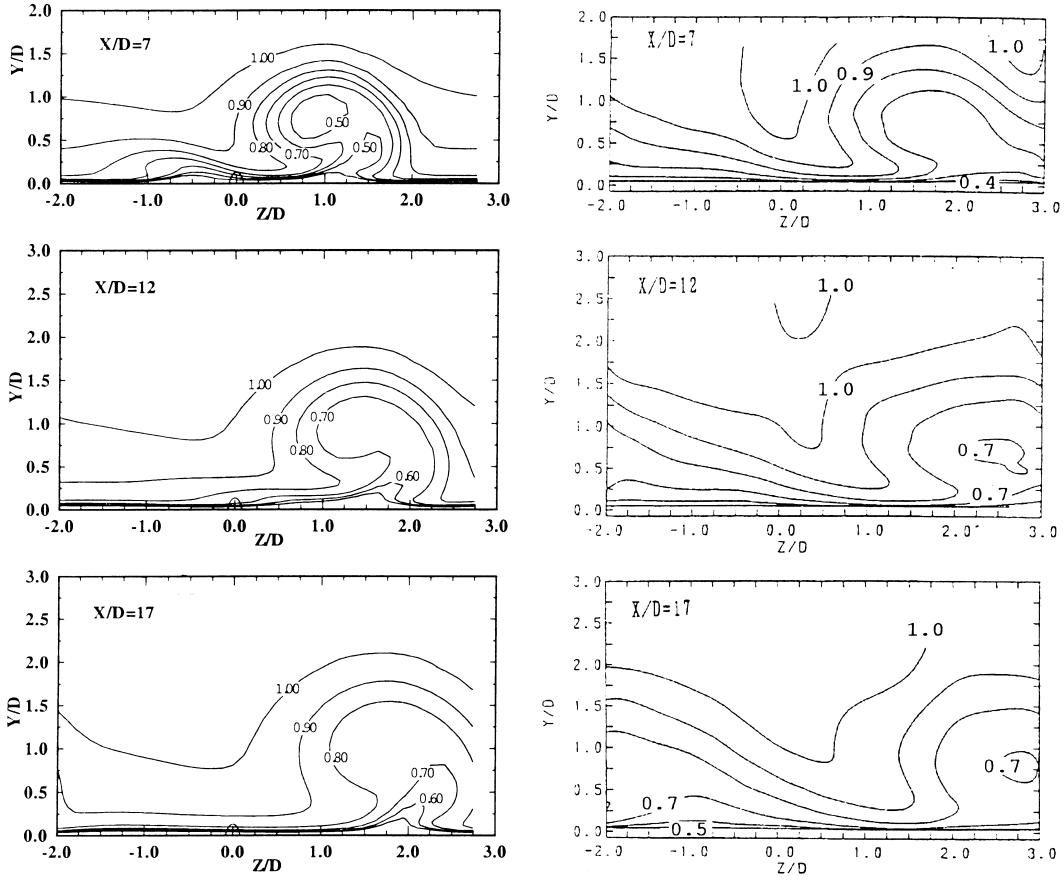

Fig. 8. U-contours; left: calculated; right: experimental $M = 0.85$; k–ε two-layer.

(reduction by only 3 orders). A typical run took almost 2 h (around 4000 iterations) on the same machine. The rate of convergence could certainly be improved by using a multigrid method.

4. Grids and boundary conditions

The computational domain with the various boundaries is shown in Fig. 2. Grid sensitivity studies indicated that with the standard k–ε model using wall functions, grid-independent results could be obtained with $78 \times 30 \times 30$ grid points in the x-, y- and z-directions as shown in Fig. 2. Additional grid dependence studies revealed that the finer mesh which consists of $94 \times 42 \times 42$ grid points, used for the two-layer computations was sufficient. The grids were considerably refined in the near-wall regions and in the vicinity of the injection hole. The lateral injection of coolant from a row of discrete holes leads to spanwise periodicity and consequently periodicity conditions were used at the lateral boundary planes midway between two holes. The first cells adjacent to the walls were set with respect to the criteria required for the individual near-wall treatment, i.e. using the two-layer approach, the width of the first grid-cell was set equal to $0.01D$, which corresponds to $0.5 < y^+ < 4$. The number of grid points placed in the viscosity-affected layer, i.e. where the damping function in Eq. (4) is less than 0.95, was in most regions above the surface of the flat plate typically 10–15. However, inside the discharge pipe the number of grid nodes in the viscosity-affected layer, which depends on the blowing rate M, did not exceed 7, and no attempt was made to refine the grid with increasing M. The boundary conditions employed are as follows: On the ground plate and the pipe walls, either wall functions were employed or the no-slip condition and $k = 0$ in the two-layer calculations, while at the upper boundary of the domain, a zero flux condition was employed. At the inflow boundary, a streamwise velocity profile deduced from the power-law approximation $U_{\text{in}} = U_s(y/\delta)^{1/7}$ with $\delta = 0.011m$ was applied to reproduce the measured fully turbulent boundary layer. The k and ε-profiles were specified using uniform distributions corresponding to a freestream turbulence intensity of $T_u = 5\%$ and a ratio $\mu_t/\mu = 50$. Honami et al. (1992), did not provide any information on the flow in the discharge pipe nor a detailed description of the geometrical details of the plenum-pipe injection system. Hence, in order to minimise the effect of the uncertain inflow conditions in the pipe, the inflow boundary was placed 8 diameters upstream of the discharge. In the absence of any information, the most reasonable assumption appeared to be that of developed pipe flow. This was supported later by Honami (private communication) who revealed that the discharge pipe was $33D$ long. The velocity profile at the pipe inlet was consequently determined from the usual profile for turbulent pipe flow, which reads $U_{\text{in}} = 1.26U_j(2z/D)^{1/6}$, z being the distance to the pipe wall. For simplicity here also uniform distributions of k and ε were specified, based on a turbulence intensity of $T_u = 5\%$ and a

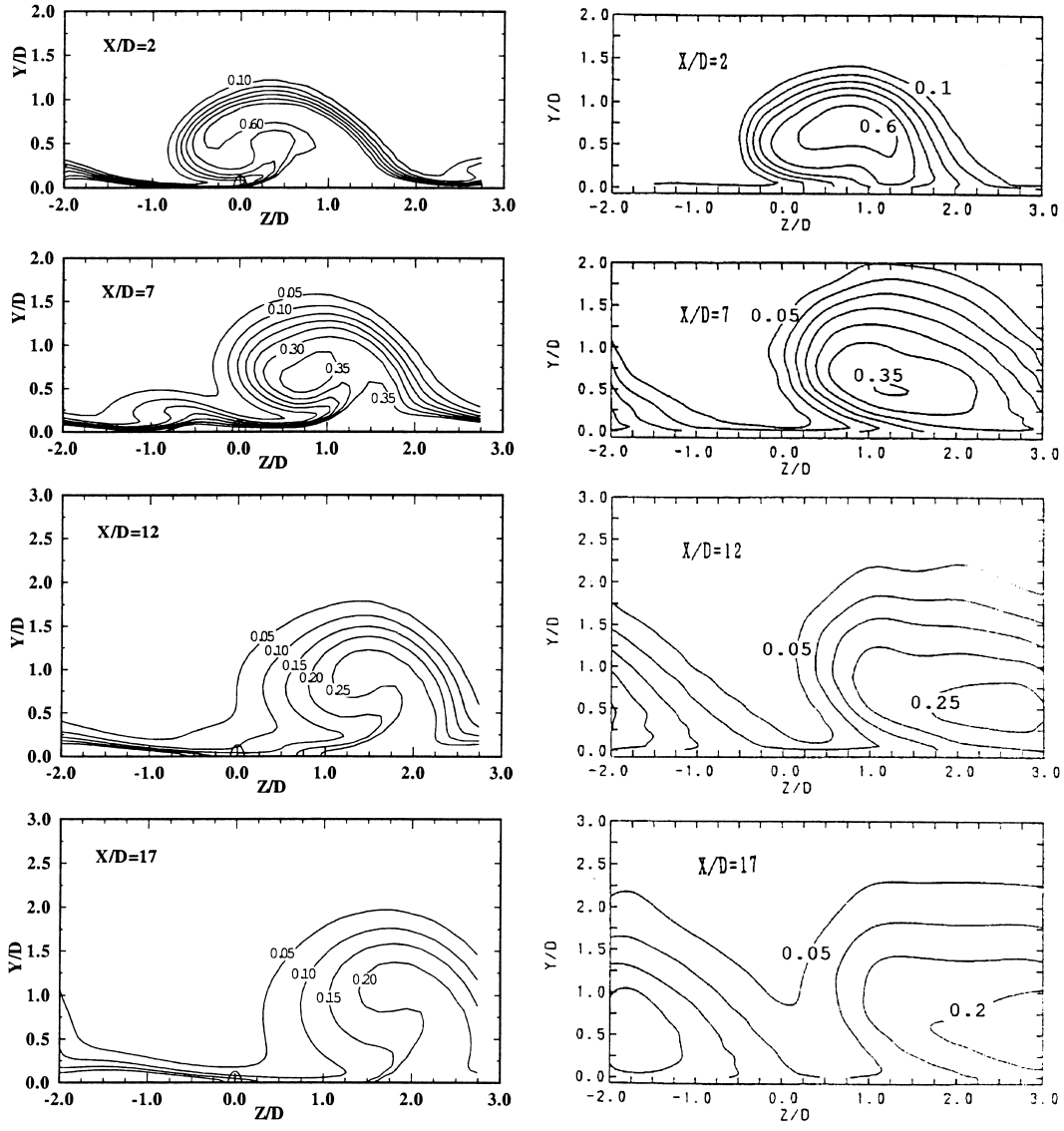

Fig. 9. η-contours; left: calculated; right: experimental $M = 0.85$; k–ε two-layer.

length scale of $k^{3/4}/\varepsilon = 0.5D$. Adiabatic wall conditions were employed when solving the enthalpy equation.

5. Results and discussion

In Figs. 3 and 4, the contours of the non-dimensional velocity U/U_∞ and temperature $\eta = (\theta - \theta_\infty)/(\theta_j - \theta_\infty)$ computed with the standard k–ε model are compared for the mass flux ratio $M = 0.5$ with the corresponding experimental data at various streamwise locations. The centre of the jet as characterised by the lowest velocities and highest temperatures can be seen to move in the spanwise injection direction with increasing streamwise distance from the hole. The injection-hole centre is located at $z = 0$ and an arrow in Fig. 4 indicates the orientation of the injection. The contours are clearly asymmetrical, with high-momentum and low-temperature fluid penetrating underneath the jet on its left side (viewed downstream). This is caused by a counter-clockwise rotating secondary-flow vortex at the left side of the jet as typically found in jets in cross flow. In jets with streamwise injection there is a counter-rotating vortex on the other side; together the two vortices cause the typical, symmetrical kidney shape of the temperature contours. In the case with lateral injection considered here, the counter-rotating vortex on the right side of the jet appears to be absent, probably because it is counteracted by the velocity of the jet and of the primary-stream fluid displaced by the jet in the spanwise (positive z) direction. Hence there is no ambient fluid pushed underneath the jet on its right side, leading to the asymmetric behaviour of the velocity and temperature contours. Due to turbulent mixing, the peak temperature in the jet decreases rapidly near the injection hole and more slowly in the downstream region. In general, the behaviour described above is predicted by the standard k–ε model in fairly good agreement with the experiments, but the model underpredicts the lateral and vertical spreading of the passive scalar and, judging from the velocity contours, the strength of the secondary-flow vortex is also underpredicted.

A qualitative illustration of the flow behaviour predicted with the two-layer model for $M = 0.5$ is shown in Fig. 5, which

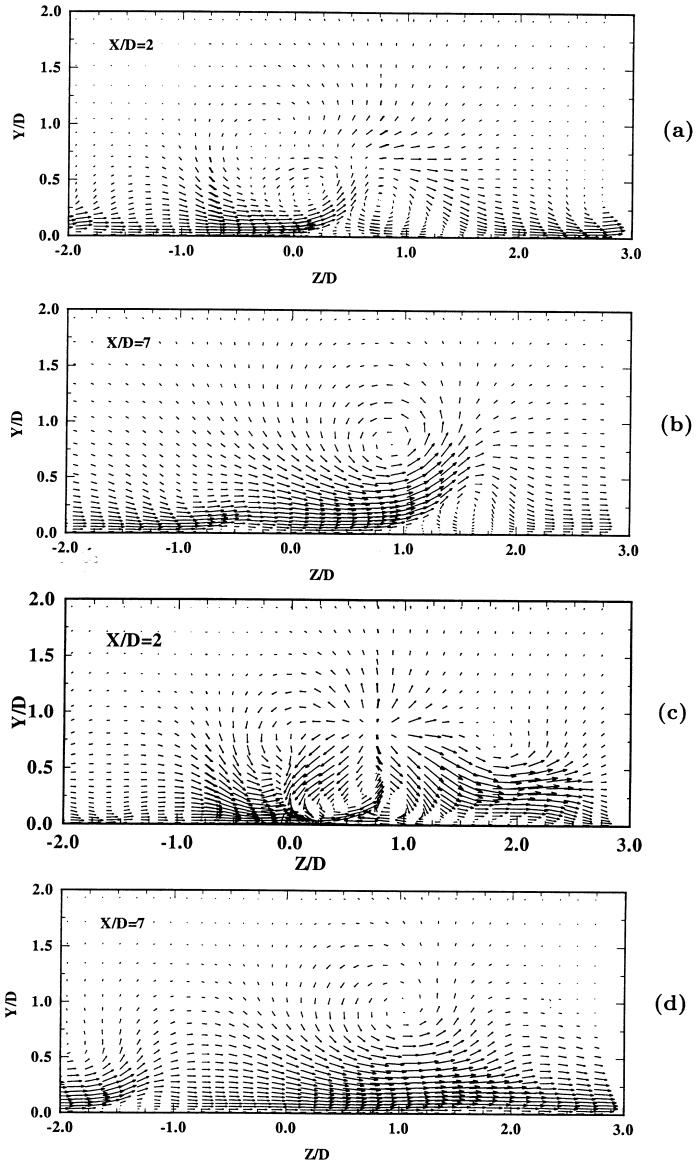

Fig. 10. Velocity vectors, v–w; $M = 0.85$, (a),(b): pure 2-l; (c),(d): 2-l ($f = 4$).

displays the flow streamlines in the immediate vicinity of the injection hole generated by following the paths of tracers injected into the oncoming and discharge flow. The figure shows the extreme complexity of the flow, especially in the direct interaction region, the formation of longitudinal vortices and the asymmetric behaviour with respect to the jet centre. The fluid-particle trajectories show also the bending-over of the jet and its shearing by the main stream on the right side, looking in the downstream direction. For the same blowing rate, Figs. 6 and 7 compare the results obtained with the two-layer model for U/U_∞ and η respectively with the experimental data. It can be seen that the model enhances the lateral spreading compared with the standard model, but the spreading in the vertical direction is suppressed. Judging again from the velocity contours, it seems that the secondary-flow vortex is more pronounced when the two-layer model is used. This results in a sharper deformation of the velocity contours predicted with this model. The η-contours clearly show more lateral diffusion of temperature which is brought about both by resolving better the important near-wall region and also promoting the strength of the secondary-flow vortex. However, the better lateral spreading is achieved at the expense of a reduced vertical spreading of temperature, and the decay of the peak temperature is now somewhat too fast in the downstream region.

Figs. 8 and 9 compare the computed and measured velocity and temperature contours for a mass flux ratio of $M = 0.85$. The calculations were obtained with the two-layer model. The velocity contours agree fairly well, even though the boundary-layer thickness on the left side of the jet is underpredicted. Closer inspection of the velocity contours at $x/D = 7$ indicates that there is more than one secondary-flow vortex present in this case. This is confirmed by the secondary-flow velocity vectors plotted at the first two stations $x/D = 2$ and $x/D = 7$ in Fig. 10(a) and (b), which show a much weaker counter-rotating vortex on the right and also traces of another

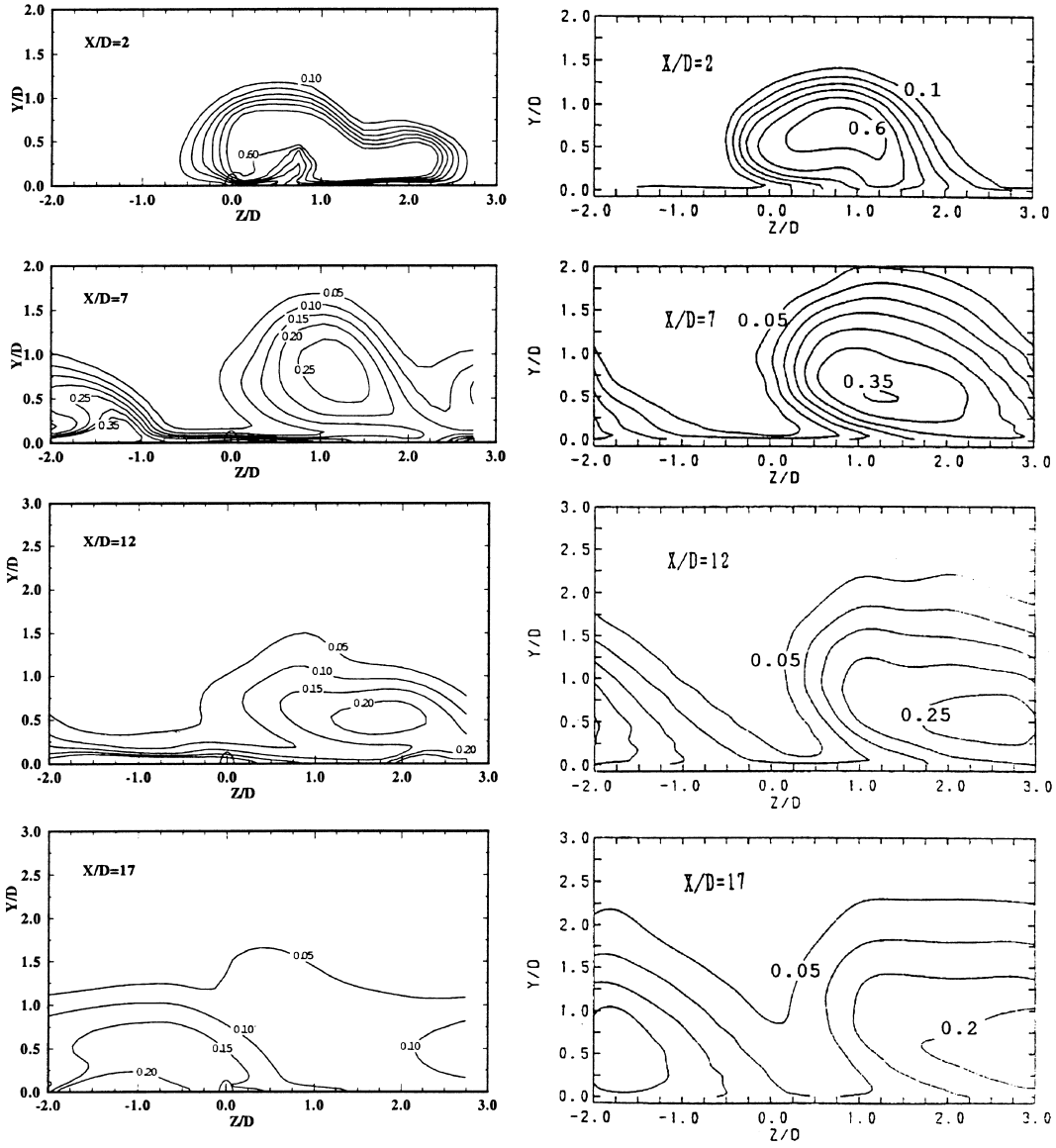

Fig. 11. η-contours; left: calculated; right: experimental $M = 0.85$; k–ε two-layer; $f = 4$.

counter-rotating vortex on the left of the main vortex (Fig. 10(b)). These additional vortices may originate from the horse-shoe vortex which the jet obstructing the oncoming boundary layer may produce. There is no indication from the experiments that these vortices exist; they may be a result of the particular turbulence model used. The temperature contours in Fig. 9 indicate that the temperature in the core is fairly well predicted but that the spanwise spreading to the right-hand side is severely underpredicted. In order to test whether the Bergeles et al modification would remove this deficiency, this case was also calculated using the formula (7) for increasing the eddy viscosity/diffusivity for the momentum and heat transfer in the lateral direction, with the factor f chosen as 4. The resulting secondary velocity vectors at $x/D = 2$ and $x/D = 7$ are shown in Fig. 10(c) and (d) and the temperature contours in Fig. 11. It can be seen that the counter-rotating vortex on the right side of the jet has disappeared and the lateral velocity at the wall is larger in this region. This, together with the increased eddy diffusivity for the lateral transport, has led to significantly increased lateral spreading of the temperature contours, at least at $x/D = 7$. There, the agreement with the measurements is fairly good, whereas it deteriorates further downstream ($x/D = 12$ and 17), and there is no clear overall improvement due to the Bergeles et al. correction, even though the lateral spreading is clearly increased. Increasing the parameter f in formula (7) by a factor of 2 (results not shown here) increases the lateral spreading a little more but does not bring a decisive improvement.

The results of the computation with the two-layer model for the case of the highest mass flux ratio ($M = 1.2$) are compared with the experiments in Figs. 12 and 13. It is clear that in this case the jet lifts off more from the wall so that the penetration of the fluid from the primary stream on the left of the jet is stronger. On the whole, this is predicted quite well by the model with roughly the correct decay in peak temperature, but

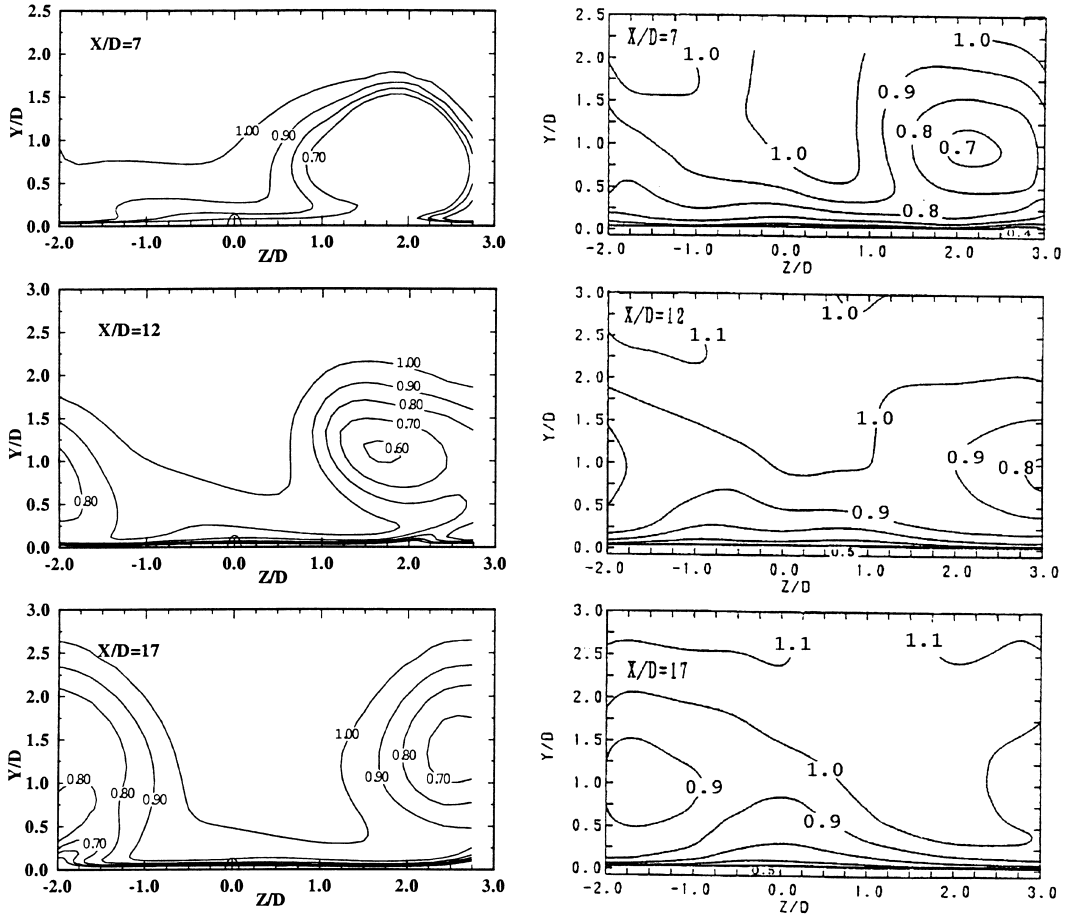

Fig. 12. *U*-contours; left: calculated; right: experimental $M = 1.20$; k–ε two-layer.

again the lateral spreading is not as strong as in the experiments.

6. Conclusions

Calculations were conducted of the 3D flow arising from lateral injection of jets into flow over a flat plate using a refined near-wall treatment. The computations underline the need for a resolution of the secondary-flow and heat-transfer mechanisms occurring in the viscosity-affected near-wall layer. Already the standard k–ε model with wall functions was found capable of capturing many of the complex features of the flow, like the asymmetric behaviour due to the injection-induced secondary-flow vortex on the left side and its absence on the right side of the jet and the initially strong and then slower decay of the temperature in the core of the jet; but the lateral jet spreading is underpredicted considerably by this model and so is somewhat also the strength of the vortex. Resolving the viscosity-affected near-wall region with a one-equation model in a two-layer approach increases the vortex strength and also the lateral spreading, but at the same time reduces the vertical spreading. In fact the strength of the secondary motion is now found to be overpredicted while the lateral spreading in the direction of the injection is still not sufficiently strong. This may be due to the use of the same eddy viscosity and diffusivity for the lateral and normal momentum and heat fluxes, while experiments have indicated that the lateral values should be higher. The Bergeles et al. (1978) correction introducing such higher viscosity/diffusivity for the momentum and heat fluxes in the lateral direction did increase the lateral spreading, but met only with partial success. It appears that further calibration of this correction is necessary since it has been developed originally only for the fully turbulent flow region and not for the viscous sublayer in which it was also used here. Of course, the correction is only a crude measure. Second-order-closure models may be necessary to cope adequately with the complex, highly non-isotropoic turbulence phenomena in the vicinity of the discharge.

The secondary-flow vortex moves primary-stream fluid underneath the coolant jet on its left side, which undermines the film-cooling effectiveness. This important process and also the decay of peak temperature could be simulated quite well by the computational model for all mass flux ratios investigated. The applications should now be extended to real blade situations.

Acknowledgements

This work was sponsored by the German Federal Ministry of Education, Science, Research and Technology through

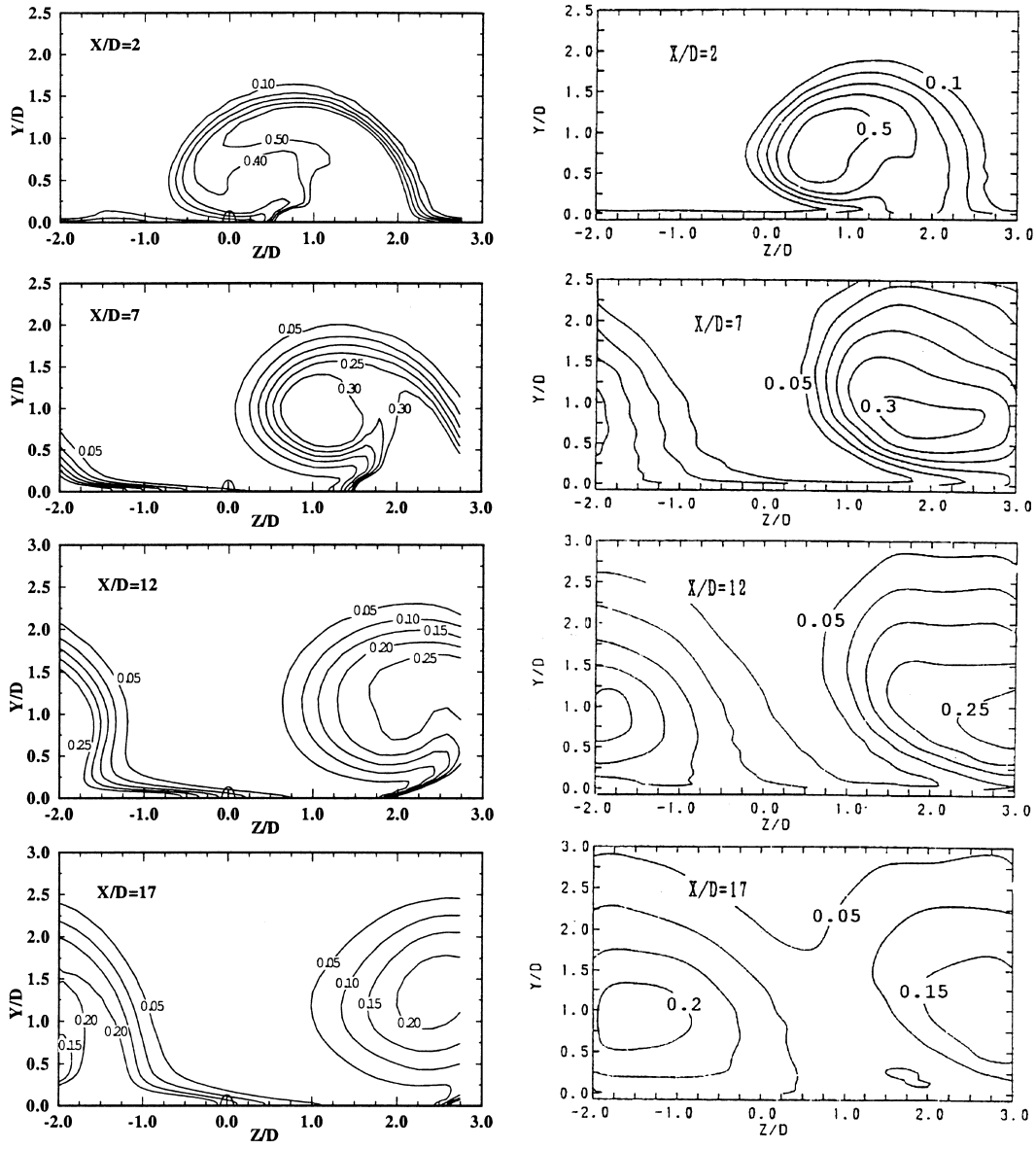

Fig. 13. η-contours; left: calculated; right: experimental $M = 1.20$; k–ε two-layer.

programme TURBOTHERM under contract No. 0326760D. The calculations were performed on the *SNI S*600/20 vector computer of the University of Karlsruhe Computer Centre.

References

Bergeles, G., Gosman, A.D., Launder, B.E., 1978. The turbulent jet in a cross stream at low injection rates: A three-dimensional numerical treatment. Numer. Heat Transfer 1, 217–242.

Demuren, A.O., Rodi, W., Schönung, B., 1985. Systematic study of film cooling with a three-dimensional calculation procedure. ASME Paper 85-IGT-2.

Honami, S., Shizawa, T., Uchiyama, A., 1992. Behaviors of the Laterally injected jet in film cooling: Measurements of surface temperature and velocity/temperature field within the jet. ASME Paper 92-GT-180.

Launder, B.E., Spalding, D.B., 1974. The numerical computation of turbulent flows. Comput. Methods Appl. Mech. Eng. 3, 269–289.

Leonard, B.P., 1979. A stable and accurate convective modelling procedure based on quadratic upstream interpolation. Comput. Methods Appl. Mech. Eng. 19, 59–98.

Majumdar, S., Rodi, W., Zhu, J., 1992. Three-dimensional finite-volume method for incompressible flows with complex boundaries. J. Fluid Eng. 114, 496–503.

Norris, L.H., Reynolds, W.C., 1975. Turbulent channel flow with a moving wavy boundary. Report No. FM-10, Stanford University, Dept. Mechanical Engineering.

Rhie, C.M., Chow, W.L., 1983. A numerical study of the turbulent flow past an isolated airfoil with trailing edge separation. AIAA J. 21, 1225–1532.

Rodi, W., 1991. Experience with two-layer models combining the k–ε model with a one-equation model near the wall. Paper AIAA 91-0216.

Stone, H.L., 1968. Iterative solution of implicit approximations of multidimensional partial differential equations. SIAM J. Numer. Anal. 5, 530–558.

Van Doormal, J.P., Raithby, G.D., 1984. Upstream weighted differencing schemes and their application to elliptic problems involving fluid flow. Comput. Fluids 2, 191–220.

Zhu, J., 1991. A low-diffusive and oscillating-free convective scheme. Comm. Appl. Numer. Methods 7, 225–232.

Zhou, J.M., Salcudean, M., Gartshore, I.S., 1993. Prediction of film cooling by discrete hole injection. ASME Paper 93-GT-75.